Available online at www.sciencedirect.com
ScienceDirect
Nuclear Physics B Proceedings Supplement 00 (2012) 1–13
Nuclear Physics B Proceedings Supplement

Cross Sections and Structure Functions at Low and Medium Q^2

Prabhdip Kaur Devgun for the H1 and ZEUS Collaborations

Panjab University Chandigarh, India, 160014

Abstract

H1 and ZEUS combined cross sections are presented in the low to medium Q^2 range. The $e^{\pm}p$ scattering data used for the combination were collected during the period 1994-2000. The combined neutral and charged current data are used as input for a NLO QCD analysis which determines a new set of parton distribution functions HERAPDF1.0 with small experimental uncertainties. In addition, recent structure function measurements from H1 and ZEUS are also presented.

Keywords: DIS, NC, CC, ZEUS, H1, HERA, QCD, F_2, F_L, PDF, Q^2, x, y, MC

1. Introduction

Deep inelastic scattering (DIS) at HERA has been central to the exploration of proton structure and quark-gluon interaction dynamics as prescribed in perturbative Quantum Chromodynamics (pQCD). HERA allowed inelastic ep interactions to be studied at high centre-of-mass energy, $\sqrt{s} \simeq 320\,\text{GeV}$, where $s = 4E_eE_p$, the lepton beam energy $E_e \simeq 27.5\,\text{GeV}$ and the proton beam energy $E_p = 920\,\text{GeV}$ for most of the running period. The HERA operation proceeded in two phases, HERA I, from 1992 – 2000, and HERA II, from 2002 – 2007. The luminosity collected by each of the collider experiments, H1 and ZEUS, in unpolarized e^+p and e^-p scattering during the first phase was approximately $100\,\text{pb}^{-1}$ and $15\,\text{pb}^{-1}$, respectively. This has allowed precision measurements of inclusive neutral (NC) and charged (CC) current DIS cross sections, which lead to a better understanding of QCD and the structure of the proton. HERA has also been operated with different proton beam energies. Before its end, the proton beam energies were lowered to allow a direct F_L measurement. The proton beam energies were lowered to 460 GeV and 575 GeV, while the electron[1] beam energy was kept constant at 27.52 GeV.

In these proceedings, combined H1 and ZEUS results are reviewed [1]. The cross sections used for the combination [2, 3, 4, 5, 6, 7, 8, 9, 10, 11, 12, 13, 14, 15] cover a wide range[2,3] of negative four-momentum-transfer squared, Q^2, and Bjorken x. The combination is performed using a method introduced in [16] and extended in [2]. The correlated systematic uncertainties and global normalizations are fitted such that one coherent data set is obtained. Since H1 and ZEUS have employed different experimental techniques, using different detectors and methods of kinematic reconstruction, the combination leads to a significantly reduced uncertainty.

The direct simultaneous measurements of the structure functions F_2 and F_L together with $R = F_L/(F_2 - F_L)$ with H1 and ZEUS data are also presented in the region $x \leq 0.001$. In the past the longitudinal structure function, or the equivalent cross section ratio R, was measured in fixed target lepton-nucleon scattering experiments [17, 18, 19, 20] in regions of large $x \geq 0.05$. The presented F_L measurements constrain the gluon density in the low x region.

[1] In this report, the term electron is used for both electrons and positrons, unless otherwise stated.

[2] $6 \cdot 10^{-7} \leq x \leq 0.65$ and $0.045 \leq Q^2 \leq 30000\,\text{GeV}^2$ for NC

[3] $1.3 \cdot 10^{-2} \leq x \leq 0.40$ and $300 \leq Q^2 \leq 30000\,\text{GeV}^2$ for CC

2. DIS Cross Sections and Structure Functions

DIS at HERA can proceed either via the NC interactions (through the exchange of a virtual photon, γ^* or Z^0), or via the CC interactions (through the exchange of a $W^{\pm}$). The DIS kinematics can be described in terms of the Bjorken scaling variable, x, the negative four momentum squared of the exchanged boson, Q^2, and the fraction of energy transferred from the lepton to the proton system (in the proton rest frame), y. For a given centre-of-mass energy squared s they are related as $Q^2 = sxy$, hence only two of them are independent.

The inclusive $e^{\pm}p$ NC[4] deep inelastic scattering (DIS) cross section can be expressed at low virtuality of the exchanged boson, Q^2, in terms of the two structure functions, F_2 and F_L, as

$$\frac{d^2\sigma^{e^{\pm}p}}{dxdQ^2} = \frac{2\pi\alpha^2 Y_+}{xQ^4}\left[F_2(x,Q^2) - \frac{y^2}{Y_+}F_L(x,Q^2)\right] = \frac{2\pi\alpha^2 Y_+}{xQ^4}\,\tilde{\sigma}(x,Q^2,y)\,, \quad (1)$$

where $Y_+ = 1 + (1-y)^2$. The quantity $\tilde{\sigma}$ is referred to as the reduced cross section. The magnitude of F_L is proportional to the absorption cross section of longitudinally polarized virtual photons by protons, $F_L \propto \sigma_L$, while F_2 includes also the absorption cross section for transversely polarized virtual photons, $F_2 \propto (\sigma_T + \sigma_L)$. The structure functions, depending on x and Q^2, are directly related to proton parton distribution functions (PDFs), and the Q^2 evolution of the structure functions is given by pQCD. F_2 dominates the ep scattering cross section for most of the kinematic region,while the structure function F_L is important only in the low Q^2 and high y (low x) kinematic region and can directly access the gluon density inside the proton.

3. Combination of the Measurements

3.1. Data Samples

In the first years until 1997, the proton beam energy E_p was set to 820 GeV. In 1998 it was increased to 920 GeV. The NC data cover a wide range in x and Q^2. The lowest Q^2 data come from the measurements of ZEUS using the BPC and BPT [7, 8]. The Q^2 range from 0.2 GeV^2 to 1.5 GeV^2 is covered using special HERA runs, in which the interaction vertex position was shifted forward allowing for larger angles of the backward scattered electron to be accepted [2, 9, 21]. The lowest Q^2 for the shifted vertex data was reached using events in which the effective electron beam energy was reduced by initial state radiation [2]. Values of Q^2 down to 1.5 GeV^2 were measured using the nominal vertex settings. For $Q^2 \leq 10$ GeV^2 the cross section is very high, and data were collected using dedicated trigger setups [2, 10, 22]. The highest accuracy of the cross section measurement is achieved for $10 \leq Q^2 \leq 100$ GeV^2 [3, 10, 22]. For $Q^2 \geq 100$ GeV^2, the statistical uncertainty of the data becomes relatively large. The high Q^2 data included in [1] were collected with positron [4, 10, 6, 14] and with electron [5, 12] beams. The NC data used for calculating the combined cross sections in [1] are listed in Table 1.

Data Set/Years		x Range		Q^2 Range GeV^2		$\mathcal{L}$ pb^{-1}
H1 svx-mb	95-00	$5\cdot10^{-6}$	0.02	0.2	12	2.1
H1 low Q^2	96-00	$2\cdot10^{-4}$	0.1	12	150	22
H1 NC	94-97	0.0032	0.65	150	30000	35.6
H1 NC	98-99	0.0032	0.65	150	30000	16.4
H1 NC HY	98-99	0.0013	0.01	100	800	16.4
H1 NC	99-00	0.0013	0.65	100	30000	65.2
ZEUS BPC	95	$2\cdot10^{-6}$	$6\cdot10^{-5}$	0.11	0.65	1.65
ZEUS BPT	97	$6\cdot10^{-7}$	0.001	0.045	0.65	3.9
ZEUS SVX	95	$1.2\cdot10^{-5}$	0.0019	0.6	17	0.2
ZEUS NC	96-97	$6\cdot10^{-5}$	0.65	2.7	30000	30.0
ZEUS NC	98-99	0.005	0.65	200	30000	15.9
ZEUS NC	99-00	0.005	0.65	200	30000	63.2

Table 1: H1 and ZEUS NC data sets, combination of these data sets along with that of the CC data sets listed in Table 2 are used as the sole input to HERAPDF1.0. The H1 svx-mb [2] and H1 low Q^2 [3] data sets comprise averages including data collected at $E_p = 820$ GeV [21, 22] and $E_p = 920$ GeV.

3.2. Combination Method

The combination of the data sets uses the χ^2 minimization method described in [2]. The χ^2 function takes into account the correlated systematic uncertainties for the H1 and ZEUS cross section measurements. For a single data set the χ^2 is defined as

$$\chi^2_{\rm exp}(\mathbf{m},\mathbf{b}) = \sum_i \frac{\left[m^i - \sum_j \gamma^i_j m^i b_j - \mu^i\right]^2}{\delta^2_{i,\rm stat}\,\mu^i\left(m^i - \sum_j \gamma^i_j m^i b_j\right) + \left(\delta_{i,\rm uncor}\,m^i\right)^2} + \sum_j b_j^2\,. \quad (2)$$

Here μ^i is the measured value at a point i, and γ^i_j, $\delta_{i,\rm stat}$ and $\delta_{i,\rm uncor}$ are the relative correlated systematic, relative statistical and relative uncorrelated systematic uncertainties, respectively. The function $\chi^2_{\rm exp}$ depends on the predictions m^i for the measurements (denoted as the

[4] in the low to medium Q^2 range, the CC cross sections can be neglected and hence will not be discussed in this review.

vector **m**) and the shifts b_j (denoted as the vector **b**) of the correlated systematic error sources. For the reduced cross section measurements $\mu^i = \sigma_r^i$, i denotes a (x, Q^2) point, and the summation over j extends over all correlated systematic sources. The predictions m^i are given by the assumption that there is a single true value of the cross section corresponding to each data point i and each process, neutral or charged current e^+p or e^-p scattering.

Equation 2 takes into account that the quoted uncertainties are based on measured cross sections, which are subject to statistical fluctuations. Under the assumption that the statistical uncertainties are proportional to the square root of the number of events and that the systematic uncertainties are proportional to **m**, the minimum of Eq. 2 provides an unbiased estimator of **m**.

Several data sets providing a number of measurements are represented by a total χ^2 function, which is built from the sum of the $\chi^2_{\rm exp}$ functions for each data set e:

$$\chi^2_{\rm tot} = \sum_e \chi^2_{{\rm exp},e} \,. \tag{3}$$

The data averaging procedure allows the rearrangement of Eq. 3 such that it takes a form similar to Eq. 2.

$$\begin{aligned}\chi^2_{\rm tot}\,(\mathbf{m}, \mathbf{b'}) = \chi^2_{\rm min} \\ + \sum_{i=1}^{N_M} \frac{\left[m^i - \sum_j \gamma_j^{i,{\rm a}} m^i b'_j - \mu^{i,{\rm a}}\right]^2}{\delta^2_{i,{\rm a,s}}\,\mu^{i,{\rm a}}\left(m^i - \sum_j \gamma_j^{i,{\rm a}} m^i b'_j\right) + \left(\delta_{i,{\rm a,u}}\, m^i\right)^2} \\ + \sum_j (b'_j)^2 \,. \end{aligned} \tag{4}$$

Here $\mu^{i,{\rm a}}$ is the average value at a point i and $\gamma_j^{i,{\rm a}}$, $\delta_{i,{\rm a,s}}$ and $\delta_{i,{\rm a,u}}$ are its relative correlated systematic, relative statistical and relative uncorrelated systematic uncertainties, respectively. The value of $\chi^2_{\rm min}$ corresponds to the minimum of Eq. 3. The ratio $\chi^2_{\rm min}/n_{\rm dof}$ is a measure of the consistency of the data sets. The number of degrees of freedom, $n_{\rm dof}$, is calculated as the difference between the total number of measurements and the number of averaged points N_M. The systematic uncertainties b'_j are obtained from the original ones, b_j, by an orthogonal transformation [2]. The summation over j extends over all independent systematic error sources. The systematic uncertainties are treated as independent between H1 and ZEUS apart from the 0.5% overall normalization uncertainty.

3.2.1. Extrapolation to Common (x, Q^2) Grid

Prior to the combination, the H1 and ZEUS data are transformed to a common grid of (x, Q^2) points. The grid points are chosen such that the interpolation corrections are minimal taking advantage of the fact that the original (x, Q^2) grids of the H1 and ZEUS experiments are similar. Furthermore, the chosen grid ensures that no two separate measurements of the same data set interpolate to a common grid point[5]. For $Q^2 \geq 0.2$ GeV^2, for the majority of the grid points both H1 and ZEUS measurements enter the combination. For some of the grid points there is no nearby counterpart from the other experiment, giving points in the combined cross section which originate from either H1 or ZEUS only. Note that through the systematic error correlation, such data points may be nevertheless shifted with respect to the original measurement in the averaging procedure.

The transformation of a measurement from the given (x, Q^2) to the nearest $(x_{\rm grid}, Q^2_{\rm grid})$ point on the grid is performed by multiplying the measured cross section by a ratio of theoretically calculated double differential cross sections at $(x_{\rm grid}, Q^2_{\rm grid})$ and (x, Q^2). This interpolation is repeated iteratively. For the first iteration, the H1 PDF 2000 parametrization [6] is used for $Q^2 \geq 3$ GeV^2, where it is applicable, and the fractal model fit [2] for $Q^2 < 3$ GeV^2. For the second iteration, a QCD fit to the first iteration of the averaged data is used for $Q^2 \geq 3$ GeV^2 and the fractal model fit for $Q^2 < 3$ GeV^2. The difference between cross section measurements obtained after the first and second iterations is smaller than a few per mille for the NC data. The QCD fit obtained using the data from the first iteration is to per mille precision identical to the fit obtained using the data from the second iteration. Therefore, no further iterations are performed. This procedure is checked using the ZEUS-JETS parametrization [23] for the first iteration. The resulting cross section difference is negligible compared to the experimental precision.

3.2.2. Centre-of-Mass Energy Correction

The data sets considered for the combination contain sub-samples taken with a proton beam energy of E_p = 820 GeV and E_p = 920 GeV. The NC scattering reduced cross sections depend weakly on the energy via terms containing the inelasticity y. For $y < 0.35$, the uncertainty on the theoretically estimated difference between cross sections for E_p = 820 GeV and E_p = 920 GeV is negligible compared to the experimental precision. Therefore the data are corrected to a common centre-of-mass energy corresponding to E_p = 920 GeV and

[5] An exception is made for the ZEUS SVX [9] data for which five pairs of points are first averaged using statistical uncertainties and then added to the combination.

then averaged. The NC data for $y \geq 0.35$ are kept separate for the two proton beam energies. The correction is calculated additively for the NC data which is quoted in reduced double differential form

$$\sigma^{th,\pm}_{r,NC920} = \sigma^{th,\pm}_{r,NC820} + \Delta\sigma^{th,\pm}_{r,NC}(x, Q^2, y_{820}, y_{920}) \,.$$

Here y_{820} and y_{920} are the inelasticities for the two proton beam energies calculated as $y = Q^2/4E_eE_px$. The theoretical cross sections follow the same prescription used for the extrapolation correction in section 3.2.1. For the neutral current cross sections in the low to medium Q^2 range

$$\Delta\sigma^{th,\pm}_{r,NC}(x, Q^2, y_{820}, y_{920}) = F^{th}_L(x, Q^2)\left[\frac{y^2_{820}}{Y_{+\,820}} - \frac{y^2_{920}}{Y_{+\,920}}\right]$$

where $Y_{+\,820,920} = 1 + (1 - y_{820,920})^2$.

To estimate the uncertainty on the combined data arising from the centre-of-mass energy correction another average is performed assuming $F^{th}_L = 0$. The difference between this and the nominal average is at most 0.1%, and thus the uncertainty on the averaged cross section resulting from the centre-of-mass energy correction is negligible.

3.2.3. Procedural Uncertainties

The χ^2 function given by equation 2 treats all systematic uncertainties as multiplicative, i.e. proportional to the expected central values. While this generally holds for the normalization uncertainties, this may not be the case for the other uncertainties. To study the sensitivity of the average result on this issue, an alternative averaging is performed, for which only normalization uncertainties are taken as multiplicative while all other uncertainties are treated as additive. The difference between this average and the nominal average result is used as a correlated procedural error $\delta_{\text{ave,rel}}$. The typical size of $\delta_{\text{ave,rel}}$ is below 0.5% for the low Q^2 data reaching a few percent for high Q^2.

The H1 and ZEUS collaborations use similar methods for detector calibration and employ similar Monte Carlo (MC) simulation models for radiative corrections, for the hadronic final state simulation and for photoproduction background subtraction. Such similarities may lead to correlations between the H1 and ZEUS measurements. To investigate the effect of possible correlations, 12 sources of similar systematic uncertainties of the two experiments are identified. These are related to the photoproduction background, the electromagnetic and hadronic energy scales and the electron scattering angle. Then 2^{12} different averages are calculated assuming each of the 12 pairs to be correlated or uncorrelated, and these alternative averages are compared to the nominal average for which all sources are assumed to be uncorrelated. By studying these averages it is found that the only two systematic sources which result in significantly different average cross sections are the photoproduction background and the hadronic energy scale. The differences between the nominal average and the averages in which systematic sources for the photoproduction background and hadronic energy scale are considered to be correlated are taken as additional procedural uncertainties $\delta_{\text{ave},\gamma p}$ and $\delta_{\text{ave,had}}$. Typical values of $\delta_{\text{ave},\gamma p}$ and $\delta_{\text{ave,had}}$ are below 0.5%. As expected, $\delta_{\text{ave},\gamma p}$ is larger at high $y > 0.5$ while $\delta_{\text{ave,had}}$ is significant for low y only.

3.2.4. Combined Results and HERAPDF1.0

The absolute normalization of the combined data set is to a large extent defined by the most precise measurements of NC e^+p cross section in the $10 \leq Q^2 \leq 100$ GeV^2 kinematic range. Here the H1 [3] and ZEUS [10] results move towards each other and the other data sets follow this adjustment. The influence of several correlated systematic uncertainties is reduced significantly for the averaged result. One of the two main reasons for this reduction is that H1 and ZEUS use different reconstruction methods. In addition, for certain regions of the phase space, one of the two experiments has superior precision compared to the other. For these regions, the less precise measurement is fitted to the more precise one, with a simultaneous reduction of the correlated systematic uncertainty. This reduction propagates to the other average points, including those which are based solely on the measurement from the less precise experiment. For $Q^2 \geq 100$ GeV^2 the precisions of the H1 and ZEUS measurements are about equal, and thus the systematic uncertainties are reduced uniformly. For $2.5 \leq Q^2 < 100$ GeV^2 and for $Q^2 < 1$ GeV^2 the precision is dominated by the H1 [2, 3] and by the ZEUS [8] measurements, respectively. Therefore the overall reduction of the uncertainties is smaller, and it is essentially obtained from the reduction of the correlated systematic uncertainty. The uncertainties are larger for high inelasticity $y > 0.6$ due to the photoproduction background. Combined H1 and ZEUS cross sections in the Q^2 range of $0.05 - 1.5$ GeV^2 are shown in Fig. 1.

The combined NC data mentioned in Table 1 and CC data listed in Table 2 are the sole input in a next-to-leading order (NLO) QCD PDF fit, called HERAPDF1.0. The consistency of the present input data justifies the use of the conventional χ^2 tolerance, $\Delta\chi^2 = 1$, when determining the experimental uncertainties on the HERAPDF1.0 fit. In the present analysis, the combina-

tion of the H1 and ZEUS data sets is done by a Hessian procedure [24, 25]. Thus for the central fit, the 110 systematic uncertainties which result from the ZEUS and H1 data sets are combined in quadrature, and the three sources of uncertainty which result from the combination procedure are treated by the offset method [26, 27].

The χ^2 per degree of freedom for this fit is 574/582; for a fit combining all 113 uncertainties in quadrature the χ^2 is 532 and for a fit treating all 113 by the Hessian method the χ^2 is 579. The resulting experimental uncertainties on the PDFs are small. Therefore, a thorough consideration of further uncertainties due to model assumptions and parametrization dependence is necessary, some of these will be explained in the following text.

The QCD predictions for the structure functions are obtained by solving the DGLAP evolution equations [28, 29, 30, 31, 32] at NLO in the $\overline{MS}$ scheme with the renormalization and factorization scales chosen to be Q^2. The DGLAP equations yield the PDFs at all values of Q^2 if they are provided as functions of x at some input scale Q_0^2. This scale is chosen to be $Q_0^2 = 1.9$ GeV^2 such that the starting scale is below the charm mass threshold, $Q_0^2 < m_c^2$. The heavy quark masses $m_c = 1.4$ GeV and $m_b = 4.75$ GeV are chosen following [33]. The strong coupling constant is fixed to $\alpha_s(M_Z) = 0.1176$ [34].

The HERA data have a minimum invariant mass of the hadronic system, W, of 15 GeV and a maximum x of 0.65, such that they are in a kinematic region where there is no sensitivity to target mass and large-x higher-twist contributions. A minimum Q^2 cut of $Q^2_{min} = 3.5$ GeV^2 is imposed on the data to remain in the kinematic region where perturbative QCD should be applicable.

The PDFs are parametrized at the input scale by the generic form

$$xf(x) = Ax^B(1-x)^C(1+\epsilon\sqrt{x}+Dx+Ex^2)\,.$$

The parametrized PDFs are the gluon distribution xg, the valence quark distributions xu_v, xd_v, and the u-type and d-type anti-quark distributions $x\bar{U}$, $x\bar{D}$. Here $x\bar{U} = x\bar{u}$, $x\bar{D} = x\bar{d} + x\bar{s}$ at the chosen starting scale. The central fit is found by first setting the ϵ, D and E parameters to zero (with additional constraints applied this leaves 9 free parameters) and then introducing them in the fit procedure, one at a time, to determine the best fit. The best 10 parameter fit has $E_{u_v} \neq 0$. The other ϵ, D and E parameters are then added, one at a time, to determine the best 11 parameter fit. The 11 parameter fits do not represent a significant improvement in fit quality compared to the best 10 parameter fit[6]. Model uncertainties and parametrization uncertainties of the central fit solution are evaluated by varying the input assumptions. The differences between the central fit and the fits corresponding to model variations of m_c, m_b, Q^2_{min}, etc. are added in quadrature, separately for positive and negative deviations, and represent the model uncertainty of the HERAPDF1.0 set. The variation in Q_0^2 is regarded as a parametrization uncertainty, rather than a model uncertainty. It mainly increases the PDF uncertainties of the sea and gluon at small x. Variations of other parameters and the number of terms in the polynomial $(1+\epsilon\sqrt{x}+Dx+Ex^2)$ were also employed. These variations mostly increase the PDF uncertainty at high x, but the valence PDFs at low x are also affected because of the constraint of the quark number sum rules. The differences between all these parametrization variations and the central fit are stored, and an envelope representing the maximal deviation at each x value is constructed to represent the parametrization uncertainty. The total PDF uncertainty is obtained by adding in quadrature experimental, model and parametrization uncertainties. The PDFs for valence and sea quarks along with those for gluons are shown in Fig. 2 at the Q^2 value of 1.9 GeV^2. More details about HERAPDF Fits can be found in [35].

Data Set/Years		x Range		Q^2 Range GeV^2		$\mathcal{L}$ pb^{-1}
H1 CC	94-97	0.013	0.40	300	15000	35.6
H1 CC	98-99	0.013	0.40	300	15000	16.4
H1 CC	99-00	0.013	0.40	300	15000	65.2
ZEUS CC	94-97	0.015	0.42	280	17000	47.7
ZEUS CC	98-99	0.015	0.42	280	30000	16.4
ZEUS CC	99-00	0.008	0.42	280	17000	60.9

Table 2: H1 and ZEUS CC data sets. Combination of these data along with that of the NC data sets listed in Table 1 were used as the sole input to the HERAPDF1.0.

The combined HERA I neutral current cross sections in the Q^2 range from $2 - 150$ GeV^2 are shown in Fig. 3 along with the HERAPDF1.0 fit.

4. F_2 and F_L measurements with H1 and ZEUS Detectors

Prior to the direct measurement of the proton longitudinal structure function F_L, values of F_2 at low x at HERA required assumptions to be made about F_L or were restricted to the kinematic region where the contribution from F_L was sufficiently suppressed to be neglected. Moreover, gluon distributions extracted from

[6]The largest decrease in χ^2 is $\Delta\chi^2 = -5$.

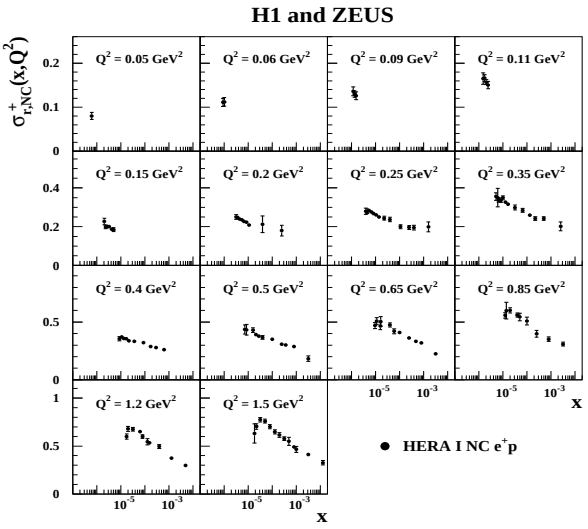

Figure 1: HERA combined NC e^+p reduced cross section at very low Q^2.

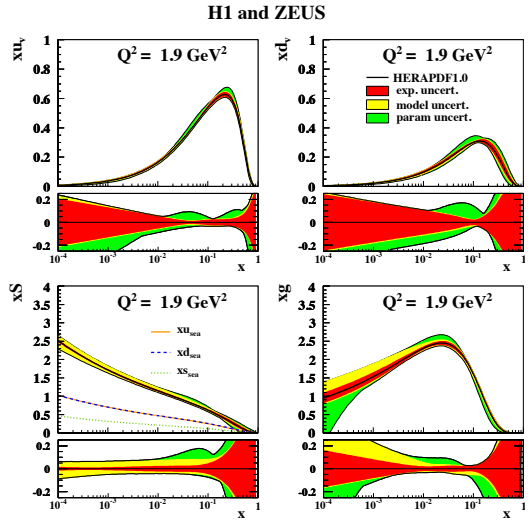

Figure 2: Parton distribution functions from HERAPDF1.0, $xu_v, xd_v, xS = 2x(\bar{U} + \bar{D})$ and xg at $Q^2 = 1.9$ GeV^2. The break-up of the Sea PDF, xS, into the flavors, $xu_{sea} = 2x\bar{u}$, $xd_{sea} = 2x\bar{d}$, $xs_{sea} = 2x\bar{s}$, is illustrated. Fractional uncertainty bands are shown below each PDF. The experimental, model and parametrization uncertainties are shown separately.

scaling violations are dependent on the formalism [36] and the order of perturbative expansion [37] used to calculate the splitting functions. Measurements of the reduced cross section at fixed (x, Q^2) and different y allow

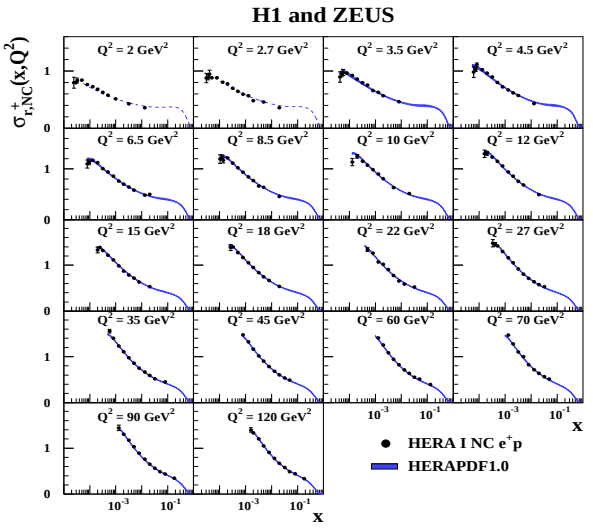

Figure 3: HERA combined NC e^+p reduced cross section at low Q^2. The HERAPDF1.0 fit is superimposed. The bands represent the total uncertainty of the fit. Dashed lines are shown for Q^2-bins not included in the QCD analysis.

F_2 and F_L to be extracted simultaneously, thereby eliminating assumptions about F_L when extracting F_2. Furthermore, a direct measurement of F_L, which is strongly correlated to the gluon density [38], provides an important consistency check of the formalism.

A model-independent determination of F_L requires the reduced cross section to be measured at fixed values of x and Q^2 for multiple centre-of-mass energies (varying y values). This method has been used previously to extract F_L in fixed-target experiments [17, 18, 19, 20] and recently by the H1 as well as ZEUS collaboration [39, 40, 41]. The H1 collaboration has also applied extrapolation methods to determine F_L [6, 22, 42].

In this review the direct ZEUS and H1 measurements of F_L and F_2 are presented. The F_2 measurements are most precise in the kinematic region where F_L is simultaneously extracted.

4.1. Experimental method

The method is based on Eq. 1, which implies that $F_2(x, Q^2) = \tilde{\sigma}(x, Q^2, y = 0)$ and $F_L(x, Q^2) = -\partial\tilde{\sigma}(x, Q^2, y)/\partial(y^2/Y_+)$, which in turn implies the need for data at fixed (x, Q^2) and different y. At HERA, this was achieved by varying $\sqrt{s}$. The precision of this procedure depends on the range available in y^2/Y_+. This was maximized by collecting data at the nominal HERA

energy, $E_p = 920$ ($\sqrt{s} = 318$ GeV), and at $E_p = 460$ ($\sqrt{s} = 225$ GeV), the lowest attainable energy with adequate instantaneous luminosity. An intermediate data set was collected at $\sqrt{s} = 251$ GeV. The data samples obtained in these runs are referred to respectively as the high- (HER), low- (LER) and medium-energy-run (MER) samples. The values of F_2 and F_L were ex-

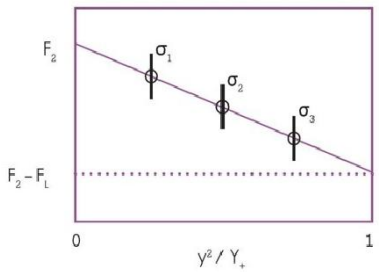

Figure 4: Diagrammatic representation of the F_L measurement at a given Q^2, x point. The points represent cross sections for the HER(σ_1), MER(σ_2) and LER(σ_3) plotted versus y^2/Y_+. The negative slope of the fit gives F_L and the intercept with the y-axis gives F_2. The HER corresponds to the lowest y and the LER corresponds to the highest y point for the F_L measurement.

tracted at fixed x and Q^2 by fitting a straight line to the values of $\tilde{\sigma}$ against y^2/Y_+ in the so-called Rosenbluth plot [43], shown in Fig. 4. For the calculation of F_L at a given (Q^2, x) the cross section at lowest y comes from the HER while the cross section at highest y comes from the LER. An event display of a typical high y event in the H1 detector is shown in Fig. 5.

4.2. Background Estimation

In the high y kinematic region the photoproduction background is more pronounced and hence needs to be subtracted. In photoproduction events, hadronic final state particles may mimic the electron signal. An event display of a typical photoproduction event observed in the ZEUS detector is depicted in Fig. 6. The main sources of background are charged hadrons (pions, kaons and anti-protons) as well as $\pi^0 \to \gamma\gamma$ decays for which one of the photons convert into an e^+e^- pair prior to entering the tracking devices. Several cuts were applied to suppress the photoproduction background. At low final state electron energies (corresponding to high y), the background contribution after the event selection is comparable to the DIS signal. In the H1 analysis two distinct methods are applied depending on the event inelasticity y. For high $y > 0.56$, the background is determined from a sample of events, in which the charge

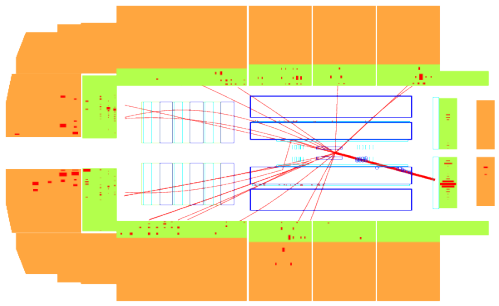

Figure 5: A high y event as reconstructed using the H1 detector; the electron trajectory is shown by a thick line and is reconstructed in the backward silicon tracker and in the inner central jet chamber. The trajectory crosses the central inner proportional chamber which is used for triggering. The hadronic final state particles are detected in the central tracker, liquid argon calorimeter and in the SpaCal electromagnetic and hadronic sections.

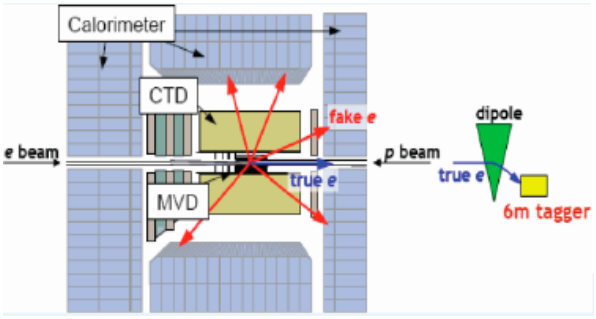

Figure 6: A high y photoproduction background event as reconstructed using the ZEUS detector. Also shown is the 6 m tagger, a detector used to tag photoproduction events. In this figure a fake electron is detected in the detector while the true scattered electron goes down the beam pipe and is detected in the 6 m tagger.

of the lepton candidate is opposite to the beam charge. For lower $y < 0.56$ the background contamination is small, however, the uncertainty due to the charge determination becomes large, and an alternative method is employed. For this sample the background is calculated from a sub-sample of events, in which the scattered lepton is detected in the electron tagger [40]. Figure 7, shows a data to MC comparison of important event variables for the LER data. The filled histogram is background (BG) determined from data, the points represent data and the band shows signal MC+BG.

In ZEUS the background is determined using the electrons detected in a detector outside the main ZEUS

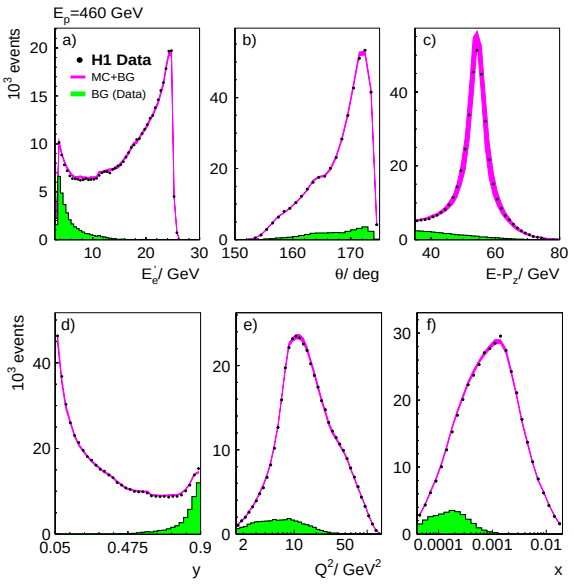

Figure 7: Distributions of the scattered electron energy $E_e\prime$ (a), polar angle θ_e (b), $E - P_z$ (c) and of the kinematic variables y (d), Q^2 (e), x (f) for events passing all analysis cuts for the $E_p = 460$ GeV sample. Data are shown as dots with statistical errors, the shaded histograms show the data driven estimation of the background and the shaded bands represent the simulation of DIS MC+BG with statistical and systematic uncertainties added in quadrature.

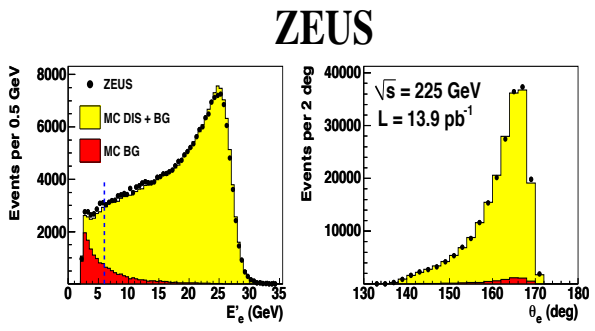

Figure 8: Distributions of the energy, E'_e, and polar angle, θ_e, of the scattered electron candidates within the LER data set compared to the combined MC predictions (MC DIS+BG). The background only MC is labeled MC BG. The vertical dashed-line represents the E'_e cut. The θ_e distributions are shown for $E'_e \geq 6$ GeV.

detector, called the 6m tagger (shown in Fig. 6), and using another independent "photoproduction enriched" sample. The amount of photoproduction background calculated by both methods was consistent with each other and is well simulated using the PYTHIA Monte Carlo. Some of the event variables for ZEUS data and MC are shown in Fig. 8 for the LER.

4.3. Extraction of F_2, F_L and R

4.3.1. ZEUS F_L Measurement

F_L has been measured in the kinematic region of $0.09 < y < 0.78$ and $20 < Q^2 < 130$ GeV^2, corresponding to $5 \cdot 10^{-4} < x < 0.007$. A direct measurement of F_2 and F_L was made possible by choosing the bins in y such that, for each of the 6 Q^2 bins, there were 3 values of x at which the reduced cross sections were measured from all three data sets. This removed the need to interpolate the data between different points in the (x, Q^2) plane. The structure functions were extracted by performing a simultaneous fit to these 54 measured cross section values using Eq. 1.

Prior to fitting, the three data sets were normalized to their luminosity-weighted average in the restricted kinematic region $y < 0.3$. To extract F_L and F_2, 48 parameters were fit simultaneously: 18 F_2 and 18 F_L values for the 18 (x, Q^2) points; 3 relative normalization factors for the HER, MER and LER data sets and 9 global shifts of systematic uncertainties [41]. The fit was performed within the BAT (Bayesian Analysis Toolkit) package [44] which, using a Markov chain MC, scans the full posterior probability density function in the 48-dimensional parameter space. ZEUS published F_2 and F_L are shown in Fig. 9. The ratio $R = F_L/(F_2 - F_L) \approx \sigma_L/\sigma_T$ and the x-averaged F_L were calculated as a function of Q^2, as shown in Fig. 10(a) and 10(b). An overall value of R was also calculated and is shown in Fig. 10(b) as a yellow band. Also shown is a comparison of the data with predictions based on the ZEUS-JETS and CTEQ6.6 [45] NLO and MSTW08 [33] NLO and NNLO[7] fits. All these predictions are based on the DGLAP formalism[8] Also shown are predictions from the NLL BFKL resummation fit from Thorne and White (TW) [48], and the prediction from the impact-parameter-dependent dipole saturation model (b-Sat) of Kowalski and Watt based on DGLAP evolution of the gluon density [49, 50, 51]. All of the models are consistent with the data.

4.3.2. H1 F_L Measurement

H1 presented its first direct F_L measurement [39] with data collected during 2006 − 2007 in a range of squared four-momentum transfers $12 \leq Q^2 \leq 90$ GeV^2 and low Bjorken x range $0.00024 \leq x \leq 0.0036$. The F_L

[7] Based on the NNLO calculations by Moch, Vermaseren and Vogt [46, 47].

[8] The conventions used for the CTEQ6.6, ZEUS-JETS and MSTW08 NLO curves are not the same, for example, F_L in CTEQ6.6 is calculated to $O(\alpha_s)$ whereas F_L in the ZEUS-JETS and MSTW08 fits are calculated to $O(\alpha_s^2)$. This accounts for most of the differences.

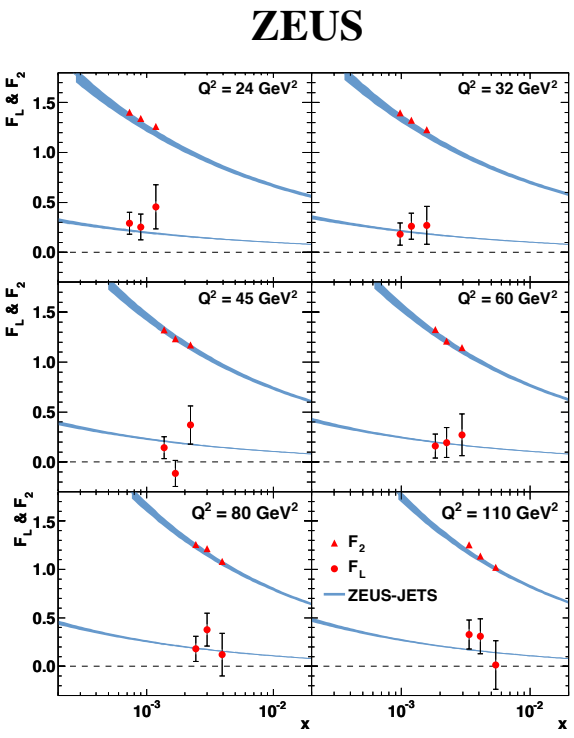

Figure 9: F_L and F_2 at 6 values of Q^2 as a function of x. The points represent the ZEUS data for F_L (•) and F_2 (▲), respectively. The error bars on the data represent the combined statistical and systematic uncertainties. The error bars on F_2 are smaller than the symbols. A further ±2.5% correlated normalization uncertainty is not included. The DGLAP-predictions for F_L and F_2 using the ZEUS-JETS PDFs [23] are also shown. The bands indicate the uncertainty in the predictions.

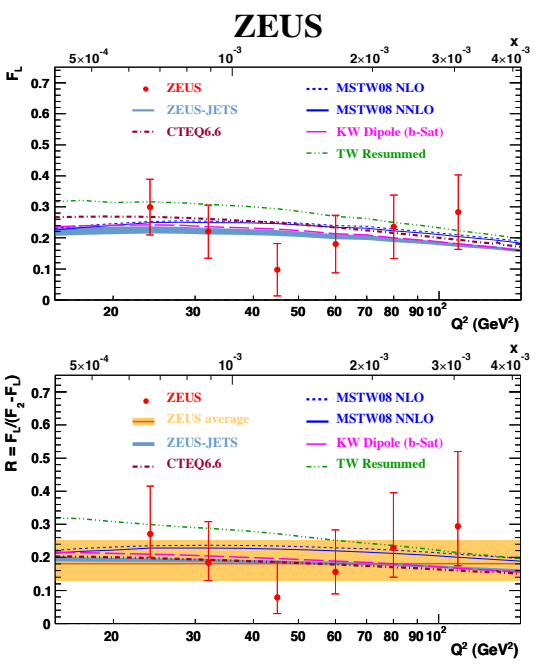

Figure 10: Values of (a) F_L and (b) R as a function of Q^2. The error bars on the data represent the combined statistical and systematic uncertainties. A further ±2.5% correlated normalization uncertainty is not included. The shaded band labeled ZEUS average represents the 68% probability interval for the overall R. The lines represent various model predictions (see text for details).

values presented in [39] were calculated using the "offset method"; i.e., F_L is calculated from a straight line fit made to the reduced cross section at different centre-of-mass energies as a function of y^2/Y_+ in each (x, Q^2) bin, and a new fit is performed for each systematic uncertainty. The overall uncertainty is determined from the collection of results.

In a recent analysis H1 has measured HER, LER and MER cross sections down to Q^2 values of 1.5 GeV^2 [40] as shown in Fig. 11. The structure function F_L was determined using the LER and MER data along with the previously published H1 HER data from [2, 3]. To determine F_L, the data measured at high y for E_p = 460 GeV are combined with the data at intermediate y for E_p = 575 GeV and low y for E_p = 920 GeV. The procedure of this F_L measurement [40] was improved as compared to [39] by including the systematic uncertainty in the fit. Thus the following χ^2 function was minimized:

$$\chi^2_0(\mathbf{F_2}, \mathbf{F_L}, \mathbf{b}) = \sum_i \frac{\left[(F_2^i - f(y^i)F_L^i) - \sum_j \Gamma^i_j b_j - \mu^i\right]^2}{\Delta_i^2} + \sum_j b_j^2 . \quad (5)$$

Here μ_i is the measured central value of the reduced cross section at a $(Q^2, x; s)$ point i with a combined statistical and uncorrelated systematic uncertainty $\Delta_i = (\Delta^2_{i,stat} + \Delta^2_{i,uncor})^{1/2}$. The effect of the correlated error sources b_j on the cross section measurements is approximated by the systematic error matrix Γ^i_j. The function χ^2_0 depends quadratically on the structure functions F_2^i and F_L^i (denoted as vectors $\mathbf{F_2}$, $\mathbf{F_L}$) as well as on b_j. Minimization of χ^2_0 with respect to these variables leads to a system of linear equations.

For low $y \leq 0.35$, the coefficient $f(y)$ is small compared to unity and thus F_L can not be accurately measured. In this kinematic domain, the constraint $0 \leq F_L \leq F_2$ provides an even better bound on the value

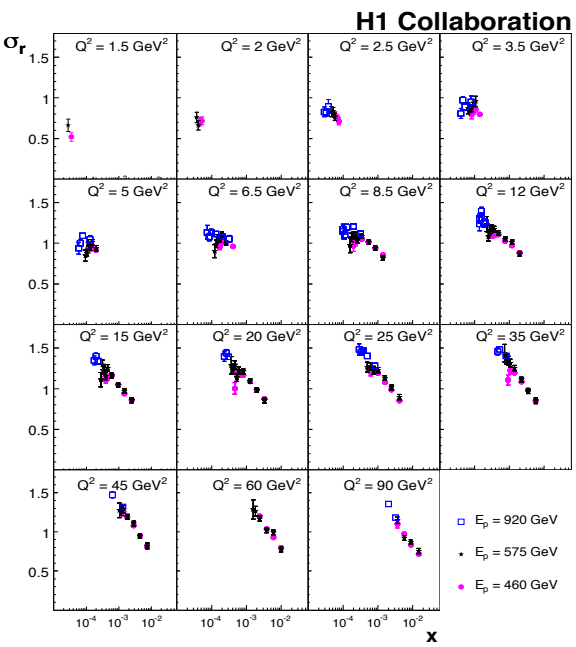

Figure 11: Results on the reduced cross section σ_r as determined from the E_p = 920 GeV, E_p = 575 GeV and E_p = 460 GeV samples. The error bars represent statistical and systematic uncertainties added in quadrature.

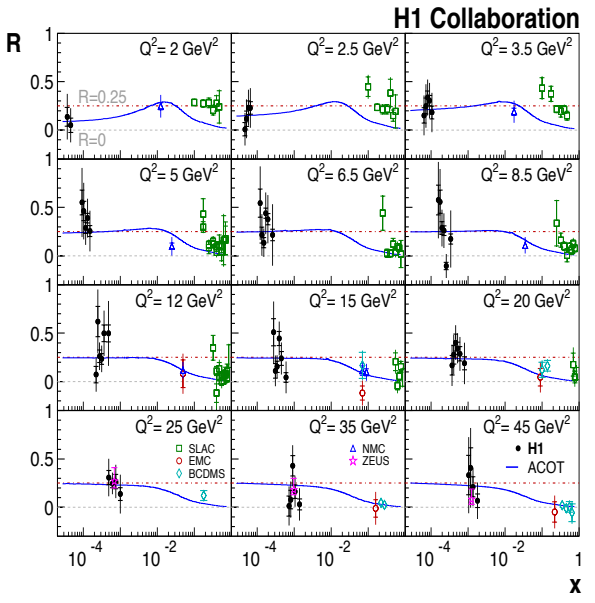

Figure 12: Ratio R as a function of x in bins of Q^2. The inner error bars represent statistical error, the full error bars include the statistical and systematic uncertainties added in quadrature. The solid curves represent predictions of the DGLAP fit in the ACOT scheme. Results from other experiments are shown by the open symbols.

of F_L than the experimental data. Furthermore, the ratio R is not expected to vary strongly as a function of x in the limited x range of sensitivity to F_L . For the kinematic range presented, it is measured to be consistent with $R \sim 0.25$ as shown in Fig. 12. To avoid unphysical values for F_L, an extra prior is introduced for the χ^2 minimization:

$$\chi^2(\mathbf{F_2}, \mathbf{F_L}, \mathbf{b}) = \chi^2_0(\mathbf{F_2}, \mathbf{F_L}, \mathbf{b}) + \sum_i \left(\frac{F_L^i - \frac{R}{R+1} F_2^i}{\Delta_{F_L}} \right), \quad (6)$$

where $R = 0.25$ and the width $\Delta_{F_L} = 3$ is chosen such that it has a negligible influence for $y > 0.35$. The additional prior preserves the quadratic dependence of the χ^2 function on F_2^i and F_L^i . The prior has a significant contribution at low y only and is very similar to imposing a common cross section normalization at low y as used in [39]. Since Δ_{F_L} is chosen to be large, the prior affects only points with large uncertainty on F_L . The bias introduced by the prior was investigated by varying the value of R between 0 and 0.5 and Δ_{F_L} between 1 and 5, and was found to be negligible for the points chosen for the F_L determination.

The measured structure function $F_L(x, Q^2)$ is shown in Fig. 13. By convention, only measurements with total uncertainties below 0.3 for $Q^2 \leq 35$ GeV^2 and below 0.4 for $Q^2 = 45$ GeV^2 are presented. The selection on the total uncertainty removes the bias due to the prior in Eq. 6. The measurement spans over two decades in x at low x, from $x = 0.00002$ to $x = 0.002$. The data are compared to the result of the DGLAP ACOT fit [52]. The structure function F_2 measured for the corresponding bins is also shown together with F_L in Fig. 13. Also included in Fig. 13 are the F_2 and F_L measurements from ZEUS [41] corrected to the Q^2 values of the current analysis using the result of the DGLAP fit in the ACOT scheme.

The values of $F_L(x, Q^2)$ resulting from averages over x at fixed Q^2 are shown in Fig. 14. The average is performed taking into account correlations. The measured structure function F_L is compared with theoretical predictions from HERAPDF1.0 [1], CT10 [53], NNPDF2.1 [54, 55], MSTW08 [33], GJR08 [56, 57] and ABKM09 [58] sets. Depending on the PDF set, the calculations are performed at NLO or NNLO in perturbative QCD. Within the uncertainties all predictions describe the data reasonably well. Figure 14 displays also the recent measurements of $F_L(Q^2)$ from ZEUS [41] which covers larger values of $Q^2 \geq 24$ GeV^2 . The data are corrected to the Q^2 values of the current analysis.

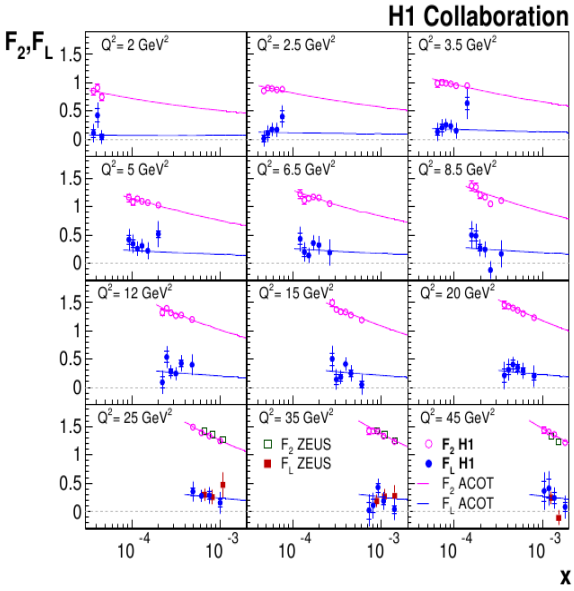

Figure 13: Proton structure functions $F_2(x, Q^2)$ and $F_L(x, Q^2)$. The inner error bars represent statistical error, the full error bars include the statistical and systematic uncertainties added in quadrature, excluding 0.5% global normalization uncertainty. The curves represent predictions of the DGLAP fit in the ACOT scheme for the structure functions F_2 and F_L . The measurements from ZEUS are also shown.

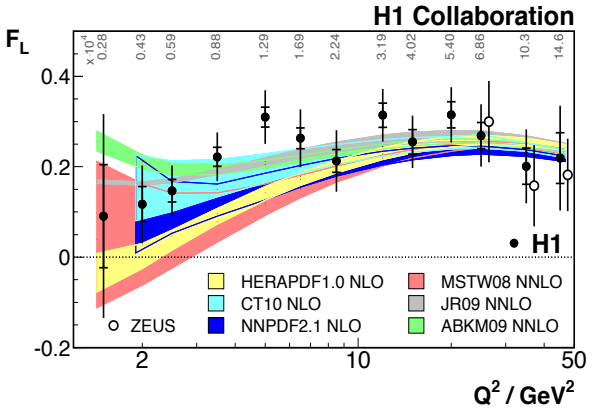

Figure 14: Proton structure function F_L shown as a function of Q^2. The average x values for each Q^2 are indicated. The inner error bars represent statistical error, the full error bars include the statistical and systematic uncertainties added in quadrature. The bands represent predictions based on HERAPDF1.0, CTEQ6.6 and NNPDF2.1 NLO as well as MSTW08, JR09 and ABKM09 NNLO calculations. The results from ZEUS are also shown by the open symbols. These data points are corrected to the Q^2 values of the current analysis and displaced for clarity.

They are in good agreement with the H1 measurement. The H1 F_L measurements presented in [40] supersede the previous published F_L [39] in the common region of phase space.

5. Extension of the ZEUS kinematic region

In a recent preliminary analysis ZEUS has extended its kinematic region coverage by using the data in the satellite as well as nominal vertex region [59]. The HERA beam structure is such that each electron bucket is separated by 60 cm from the neighboring one, whereas the corresponding separation for two consecutive proton bunches is 144.2 cm. The collision of a particle from a side bucket with a particle in the other beam results in vertices (Svtx) displaced from the nominal interaction region, as can be seen in Fig. 15. The

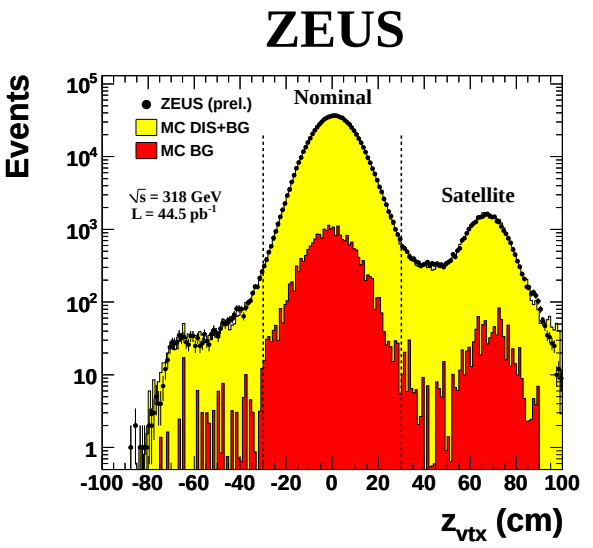

Figure 15: Distributions of the reconstructed z-vertex of the events (linear and log scale) within the HER data set compared to the combined MC predictions (MC DIS+BG). The background only MC is labeled MC BG. The two vertical dashed-lines in the figure represent the separation of nominal and satellite region.

value of Q^2 depends upon the energy and angle of the scattered electron candidate. Given the minimum energy at which the scattered electron can be reliably measured, lower values of Q^2 can only be reached if scattered electrons at larger polar angles can be measured. Scattered electrons measured at the same impact point in the backward calorimeter are found at larger polar angles for the satellite vertex around $z = +70$ cm than for the nominal vertex at $z = 0$ cm. Thus the analysis of satellite vertex collisions is a way to access lower Q^2. The data sets used for the analysis are the same as

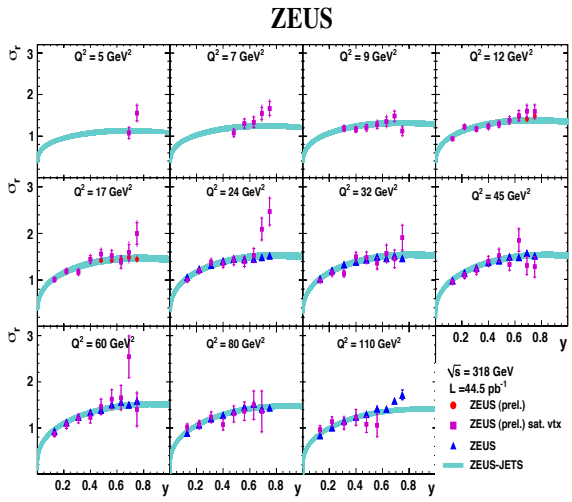

Figure 16: ZEUS preliminary cross sections for nominal vertex (•) events and satellite vertex (■) events for the HER data set. The bands show the predictions from the ZEUS-JETS PDFs [23], also shown are the ZEUS published results (▲). Inner error bars are the statistical and outer are the statistical and systematic errors added in quadrature.

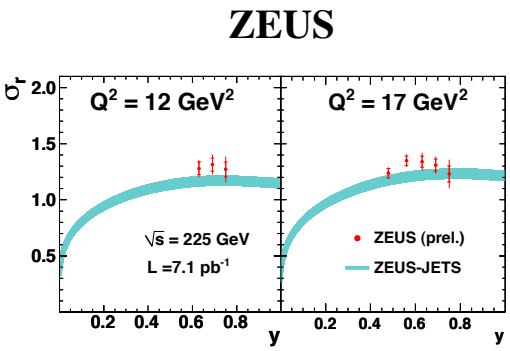

Figure 17: ZEUS preliminary cross sections for nominal vertex (•) events for the LER. The bands show the predictions from the ZEUS-JETS PDFs [23]. Inner error bars are the statistical and outer are the statistical and systematic errors added in quadrature.

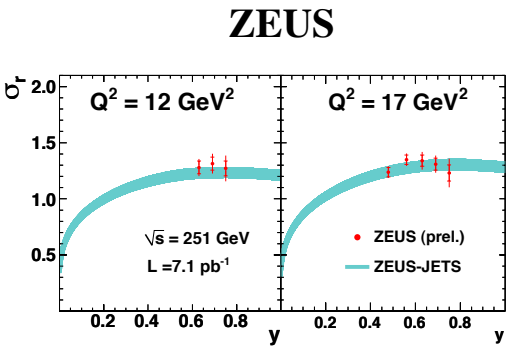

Figure 18: ZEUS preliminary cross sections for nominal vertex (•) events for the MER. The bands show the predictions from the ZEUS-JETS PDFs [23]. Inner error bars are the statistical and outer are the statistical and systematic errors added in quadrature.

those used in [41]. The z-vertex distribution is shown in Fig. 15 for the HER data set. The HER cross sections were measured down to $Q^2 = 5$ GeV^2 for HER and to $Q^2 = 12$ GeV^2 for LER and MER. The cross sections for the HER are shown in Fig. 16 along with the NLO QCD predictions using the ZEUS-JETS PDFs [23], indicating good agreement. Also shown in Fig. 16 are published ZEUS results. In the common phase space a good agreement is observed between the two measurements. The reduced cross sections in the low Q^2 region for LER and MER were calculated using the data from the nominal vertex, and the results are shown in Figs. 17 and 18 along with the predictions from the ZEUS-JETS PDFs.

ZEUS plans to use the cross section measurement in the low Q^2 range to measure F_L in the range where all HER, LER and MER cross sections are available at the same Q^2 and x.

6. Summary

ZEUS and H1 combined results for NC cross sections in the low to medium Q^2 range were reviewed. The combination improves the precision significantly. The combined CC and NC cross section measurements from all HERA I data have been used to determine HERAPDF1.0 in the $\overline{MS}$ scheme. NLO QCD calculations based on this PDF set describe the data well. The structure functions F_2, F_L and R from both experiments were also presented. The measurements are in good agreement with predictions from different PDF groups. These direct measurement of F_L and F_2 in the low to medium Q^2 and low x range are expected to lead to a better understanding of the QCD physics in this kinematic regime. The structure function F_L constraints the gluon PDFs more effectively than previously possible.

Acknowledgments

We appreciate the contributions to the construction and maintenance of the ZEUS and H1 detectors of many people who are not listed as authors. The HERA ma-

chine group and the DESY computing staff are especially acknowledged for their success in providing excellent operation of the collider and the data-analysis environment. We thank the DESY directorate for their strong support and encouragement.

References

[1] F.D. Aaron *et al.* [H1 and ZEUS Collaborations], JHEP 01 (2010) 109.
[2] F.D. Aaron *et al.* [H1 Collaboration], Eur. Phys. J. C 63 (2009) 625.
[3] F.D. Aaron *et al.* [H1 Collaboration], Eur. Phys. J. C 64 (2009) 561.
[4] C. Adloff *et al.* [H1 Collaboration], Eur. Phys. J. C 13 (2000) 609.
[5] C. Adloff *et al.* [H1 Collaboration], Eur. Phys. J. C 19 (2001) 269.
[6] C. Adloff *et al.* [H1 Collaboration], Eur. Phys. J. C 30 (2003) 1.
[7] J. Breitweg *et al.* [ZEUS Collaboration], Phys. Lett. B 407 (1997) 432.
[8] J. Breitweg *et al.* [ZEUS Collaboration], Phys. Lett. B 487 (2000) 53.
[9] J. Breitweg *et al.* [ZEUS Collaboration], Eur. Phys. J. C 7 (1999) 609.
[10] S. Chekanov *et al.* [ZEUS Collaboration], Eur. Phys. J. C 21 (2001) 443.
[11] J. Breitweg *et al.* [ZEUS Collaboration], Eur. Phys. J. C 12 (2000) 411.
[12] S. Chekanov *et al.* [ZEUS Collaboration], Eur. Phys. J. C 28 (2003) 175.
[13] S. Chekanov *et al.* [ZEUS Collaboration], Phys. Lett. B 539 (2002) 197.
[14] S. Chekanov *et al.* [ZEUS Collaboration], Phys. Rev. D 70 (2004) 052001.
[15] S. Chekanov *et al.* [ZEUS Collaboration], Eur. Phys. J. C 32 (2003) 1.
[16] A. Glazov, AIP Conf. Proc. 792 (2005) 237.
[17] J.J. Aubert *et al.*, Phys. Lett. B 121 (1983) 87.
[18] A.C. Benvenuti *et al.*, Phys. Lett. B 223 (1989) 485.
[19] L.W. Whitlow *et al.*, Phys. Lett. B 250 (1990) 193.
[20] M. Arneodo *et al.*, Nucl. Phys. B 483 (1997) 3.
[21] C. Adloff *et al.* [H1 Collaboration], Phys. Lett. B 497 (1997) 3.
[22] C. Adloff *et al.* [H1 Collaboration], Eur. Phys. J. C 21 (2001) 33.
[23] S. Chekanov *et al.* [ZEUS Collaboration], Eur. Phys. J. C 42 (2005) 1.
[24] J. Pumplin *et al.*, JHEP 0207 (2002) 012.
[25] J. Alekhin *et al.*, Phys. Rev. D 68 (2003) 014002.
[26] M. Botje *et al.*, Eur. Phys. C 14 (2000) 285.
[27] S. Chekanov *et al.* [ZEUS Collaboration], Phys. Rev. D 67 (2003) 012007
[28] V.N. Gribov and L.N. Lipatov, Sov. J. Nucl. Phys. 15 (1972) 438.
[29] V.N. Gribov and L.N. Lipatov, Sov. J. Nucl. Phys. 15 (1972) 675.
[30] L.N. Lipatov, Sov. J. Nucl. Phys. 20 (1975) 94.
[31] Y.L. Dokshitzer, Sov. Phys. JETP 46 (1977) 641.
[32] G. Altarelli and G. Parisi, Nucl. Phys. B 126 (1977) 298.
[33] A.D. Martin, W.J. Stirling, R.S. Thorne and G. Watt, Eur. Phys. J. C 63 (2009) 189.
[34] C. Amsler *et al.* (Particle Data Group), Phys. Lett. B 667 (2008) 1.
[35] K. Lipka [H1 Collaboration], these proceedings.
[36] S. Catani, Z. Phys. C 75 (1997) 665.
[37] A.D. Martin, W.J. Stirling and R.S. Thorne, Phys. Lett. B 635 (2006) 305.
[38] G. Altarelli and G. Martinelli, Phys. Lett. B 76 (1978) 89.
[39] F.D. Aaron *et al.* [H1 Collaboration], Phys. Lett. B 665 (2008) 139.
[40] F.D. Aaron *et al.* [H1 Collaboration], Eur. Phys. J. C 71 (2011) 1579.
[41] S. Chekanov *et al.* [ZEUS Collaboration], Phys. Lett. B 682 (2009) 8.
[42] C. Adloff *et al.* [H1 Collaboration], Phys. Lett. B 393 (1997) 452.
[43] M.N. Rosenbluth, Phys. Rev. 79 (1950) 615.
[44] A. Caldwell, D. Kollár and K. Kröninger, arXiv:0808.2552 [physics.data-an].
[45] P.M. Nadolsky *et al.*, Phys. Rev. D 78 (2008) 013004.
[46] S. Moch, J.A.M. Vermaseren and A. Vogt, Phys. Lett. B 606 (2005) 123.
[47] J.A.M. Vermaseren, A. Vogt and S. Moch, Nucl. Phys. B 724 (2005) 3.
[48] C.D. White and R.S. Thorne, Phys. Rev. D 75 (2007) 034005.
[49] G. Watt and H. Kowalski, Phys. Rev. D 78 (2008) 014016.
[50] H. Kowalski, L. Motyka and G. Watt, Phys. Rev. D 74 (2006) 074016.
[51] H. Kowalski and D. Teaney, Phys. Rev. D 68 (2003) 114005.
[52] M. Kramer, F.I. Olness and D.E. Soper, Phys. Rev. D 62 (2000) 096007.
[53] H. -L. Lai *et al.*, Phys. Rev. D 82 (2010) 074024.
[54] R.D. Ball *et al.*, Nucl. Phys. B 838 (2010) 136.
[55] S. Forte, E. Laenen, P. Nason and J. Rojo, Nucl. Phys. B 834 (2010) 116.
[56] M. Glück, P. Jimenez-Delgado and E. Reya, Eur. Phys. J. C 53 (2008) 355.
[57] P. Jimenez-Delgado and E. Reya, Phys. Rev. D 79 (2009) 074023.
[58] S. Alekhin, J. Blümlein, S. Klein and S. Moch, Phys. Rev. D 81 (2010) 014032.
[59] *ZEUS-prel-10-006.* [ZEUS Collaboration], (2010).